

## Article

# Early Triassic (Griesbachian) Deposits of High-Energy Events at the Northwestern Upper Yangtze Region, China

Dan Qiao <sup>1</sup>, Xiong Duan <sup>2</sup> and Zhiqiang Shi <sup>1,\*</sup>

<sup>1</sup> Institute of Sedimentary Geology, Chengdu University of Technology, Chengdu, 610059, China; jilin8819636@163.com

<sup>2</sup> School of Geographical Science, China West Normal University, Nanchong, 637002, China; duanxiong00@163.com

\* Correspondence: szqcdu@163.com

**Abstract:** Following the latest Permian mass extinction (LPME), the ocean experienced turbulent conditions due to elevated temperatures during the Griesbachian (Early Triassic). These adverse conditions resulted in a prolonged delay in biotic recovery. However, the current understanding of the sedimentological responses of the ocean at that time to these adverse conditions remains incomplete. The Griesbachian harsh ocean conditions led to the formation of abnormal carbonate rocks (known as anachronistic facies) all around the world. These facies were influenced by a combination of environmental conditions, biotic factors, and actualistic sedimentological processes (e.g., waves and currents, sedimentation). However, the role of actualistic sedimentological processes in forming anachronistic facies during the Griesbachian has been underemphasized in the existing studies. In this research, we examine calcirudite beds, such as flat-pebble conglomerates, from Member 1 of the Feixianguan Formation across multiple sections, including Shangsi, Yudongzi, Dagouli, and Jianfeng in the Upper Yangtze Region. Our analysis is grounded in field investigations, thin-section observations, and the study of triggering mechanisms and formation processes. We identified and described five calcirudite beds (S1–S5) in the Shangsi section, two beds (D1–D2) in the Dagouli section, one at Jianfeng (J1), and one (Y1) in the Yudongzi section. Bed S1 features matrix-supported flat pebbles with a normal grading, interpreted as the result of a debris flow mass-transport process. Beds S2, S3, D1, and J1 contain large mud rip-up clasts, ooids, and bioclasts, suggesting a potential link with tsunami backwash. Beds S4, D2, and Y1 display hummocky cross-stratification and ‘chrysanthemum-shaped’ flat pebbles, indicating storm influence. The presence of vermicular limestones in Bed S5 suggests harsh marine environmental conditions. Collectively, this evidence suggests that high-energy oceanic conditions, including tsunamis and frequent storms, potentially influenced Early Triassic biotic recovery.

**Keywords:** high-energy sedimentary deposits; debris flow; tsunami and storm events; flat-pebble conglomerate; Early Triassic; Yangtze



**Citation:** Qiao, D.; Duan, X.; Shi, Z. Early Triassic (Griesbachian) Deposits of High-Energy Events at the Northwestern Upper Yangtze Region, China. *Minerals* **2023**, *13*, 1222. <https://doi.org/10.3390/min13091222>

Academic Editor: János Haas

Received: 3 July 2023

Revised: 12 September 2023

Accepted: 15 September 2023

Published: 17 September 2023



**Copyright:** © 2023 by the authors. Licensee MDPI, Basel, Switzerland. This article is an open access article distributed under the terms and conditions of the Creative Commons Attribution (CC BY) license (<https://creativecommons.org/licenses/by/4.0/>).

## 1. Introduction

As the most severe biotic crisis in Phanerozoic history, the latest Permian mass extinction (LPME) was characterized by the elimination of over 90% of species in the oceans and approximately 70% of vertebrate families on land [1]. Numerous high-resolution studies of the Permian–Triassic boundary (PTB) have revealed dramatic changes in sedimentary features and fabrics, including the Early Triassic ‘coal gap’, ‘reef gap’, and ‘chert gap’ [2–4]. Shortly after the LPME, marine species experienced a delayed recovery that spanned approximately 5 million years. This delay is attributed to abnormal ocean conditions, such as high sea-surface temperatures, acidification, and anoxia [5,6]. These conditions led to the deposition of abnormal facies, characterized by the occurrence of intraformational calcirudites in shelf settings [7]. The term ‘abnormal facies’ is typically reserved for periods

during which ancient oceans experienced extraordinary environmental conditions [8]. The sedimentary record shows a diverse range of these abnormal facies, including intraclastic limestone, wrinkle structures, microbialites, carbonate seafloor precipitates, vermicular limestone, and oolites [8]. These intraclastic limestone facies, sometimes referred to as ‘anachronistic facies’ by certain authors, contain flat-pebble conglomerates, breccia, and vermicular limestone [9–11]. The deposition of these anachronistic facies is the manifestation of related environmental events following the LPME [8,11]. Understanding the genetic mechanisms and depositional settings in which these rocks formed is crucial to comprehending the processes involved in Early Triassic ecosystem reconstruction [8,11–13].

Numerous studies on Lower Triassic intraclastic limestones have been conducted in the Paleotethys and Neotethys successions, particularly in South China [4,5,9,12–14] and western North America [12,13,15–17]. Given the close relationship between the turbulent ancient ocean events and delayed recovery [18], intraclastic limestones may serve as a proxy indicator of paleo-ocean environmental changes in the Lower Triassic [7]. These intraclastic limestones developed during different periods and are attributed to various environmental or depositional factors [15–19]. They include brecciated limestone and flat-pebble conglomerates, which have been interpreted as seismites [7,20,21], gravity flow deposits [22–25], or storm layers [12,26,27]. Despite these studies, the relationship between these intraclastic limestones and marine high-energy events has not yet been sufficiently ascertained.

The Lower Triassic successions are well exposed at the Shangsi, Dagouli, Jianfeng, and Yudongzi sections along the northwestern margin of the Sichuan Basin in South China. As a candidate for the Global Stratotype Section and Point (GSSP) for the Permian–Triassic boundary (PTB), the Shangsi section preserves traces of geological events and a remarkable PTB stratum in the eastern Paleo-Tethys Ocean [7]. Strata of ramp facies in the mid-Tethys and west-Tethys, for instance, provide evidence of a substantial reduction in carbonate production and an acidification event at the extinction horizon [15]. In this study, we focus on both the macrostructure and microscopic fabric features of the calcirudites, which represent high-energy events in the Paleo-Tethys Ocean along the northwestern Upper Yangtze Region. Here, we study the anachronistic facies to better understand the source of intraclasts, triggering mechanisms, and formation processes in different beds.

## 2. Geologic and Stratigraphic Setting

The South China block, which is composed of both the Yangtze Block and Cathaysia Block [28], was located at the eastern margin of the Paleo-Tethys Ocean, near the equator, during the Early Triassic period (Figure 1A) [29]. During this period, the South China block remained geographically isolated from neighboring tectonic blocks. The western half of the Sichuan Basin corresponds with the northwestern margin of the Yangtze platform, and is situated south of the Qinling–Dabie collisional suture [30]. The modern Sichuan Basin is tectonically delineated by the Longmenshan fold belt to the northwest, adjacent to the Songpan–Ganzi block, and by the Emeishan–Liangshan fold belt to the southwest [30]. The Early Triassic Yangtze Block was principally tectonically stable, dominated by shallow water carbonate depositional environments (Figure 1B) [31,32]. The paleogeographic setting of the northwestern Sichuan Basin consisted of slope and carbonate platform facies (Figure 1C) [30,32]. The sedimentary succession in the northern Sichuan Basin includes the Upper Permian Dalong Formation, which is primarily composed of radiolarian-rich siliceous limestone and siliceous shale. This is overlain by the Lower Triassic Feixianguan Formation, comprised of shales and carbonate rocks [33]. The boundary between the Dalong and Feixianguan Formations is delineated by two distinct dark clay layers, interspersed with a yellowish-white clay layer (Figure 2). These clay beds (about  $252.28 \pm 0.13$  Ma), have been identified as tuffs [34,35] and are widely distributed in the South China Block. They are internationally acknowledged as the lithologic marker for the Permian–Triassic boundary (PTB) [35–37]. In fact, the biostratigraphic Permian–Triassic boundary (PTB) is situated a few tens of centimeters above this lithologic marker and

is identified via the presence of the conodont *Hindeodus parvus* [38–40]. In the Sichuan Basin, the Feixianguan Formation is divided into four members [41]. Member 1 is primarily composed of mudstone and limestone [42], while Members 2–4 mainly consist of massive carbonate rock as well as flaser mudstone or marl [41,43].

Member 1 of the Feixianguan Formation is found at the Shangsi, Dagouli, Jianfeng, and Yudongzi sections, which are situated along the northwestern margin of the Sichuan Basin (Figure 1C). Among these, the Shangsi section has been proposed as a Global Stratotype Section and Point (GSSP) candidate for the Permian–Triassic boundary (PTB) [33]. In the Shangsi section, the lower part of Member 1 is composed of shale and marl, while the upper part consists of limestone, calcirudites, and flat-pebble conglomerates [32]. At Dagouli, Member 1 of the Feixianguan Formation includes micrite, bioclastic limestone, marl, and a significant number of flat-pebble conglomerates belonging to slope carbonate facies [22]. In the Jianfeng section, Member 1 of the Feixianguan Formation is primarily composed of intraclast limestones (calcirudites) and marls. Finally, the Yudongzi section features carbonate facies such as microbialites, oncolitic limestones, and calcirudites [44]. Tang et al. (2016) [45] reported the first appearance of the conodont species *Hindeodus parvus* in PTB microbialites in the Yudongzi section. The calcirudite (carbonate breccia) bed mainly occurs in the *Isarcicella* Zone, which is Griesbachian in age. It should be noted that the upper part of the Upper Permian Changxing Formation at Jianfeng and Yudongzi is primarily characterized by rich coral biolithite, representative of carbonate platform facies [43].

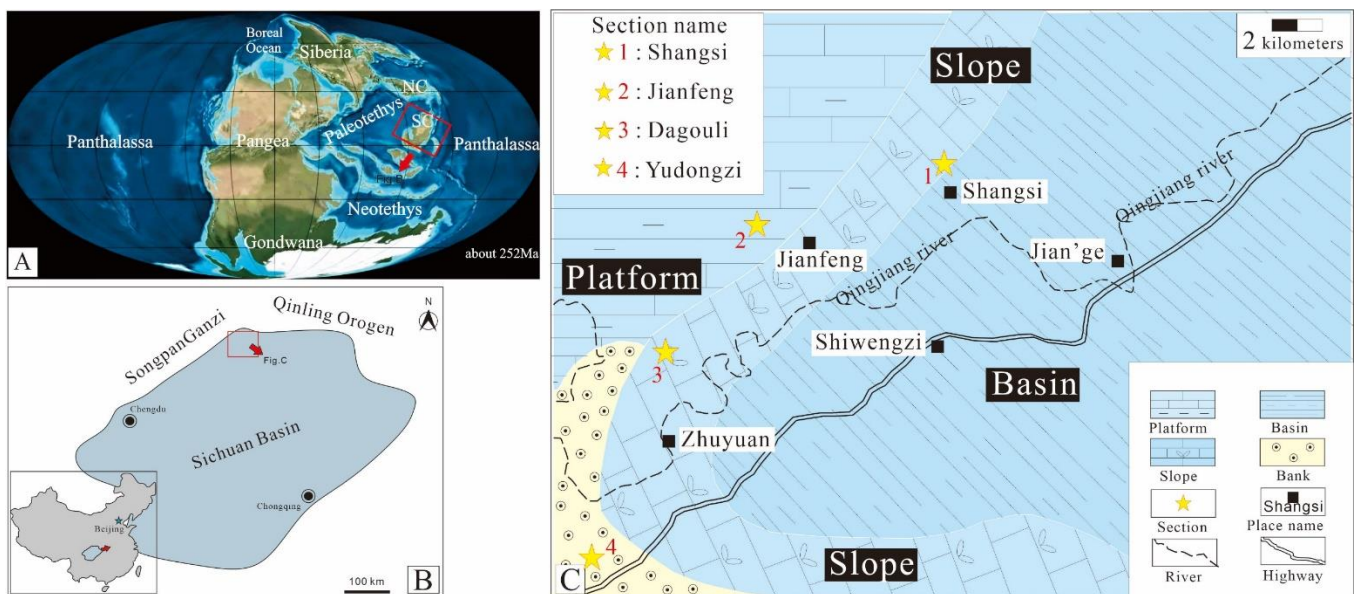


**Figure 1.** (A) Map of global Early Triassic paleogeography [46]. (B) Map of the Sichuan Basin showing the location of the studied sections [47]. (C) Palaeofacies map of the research area during the Early Triassic [30].

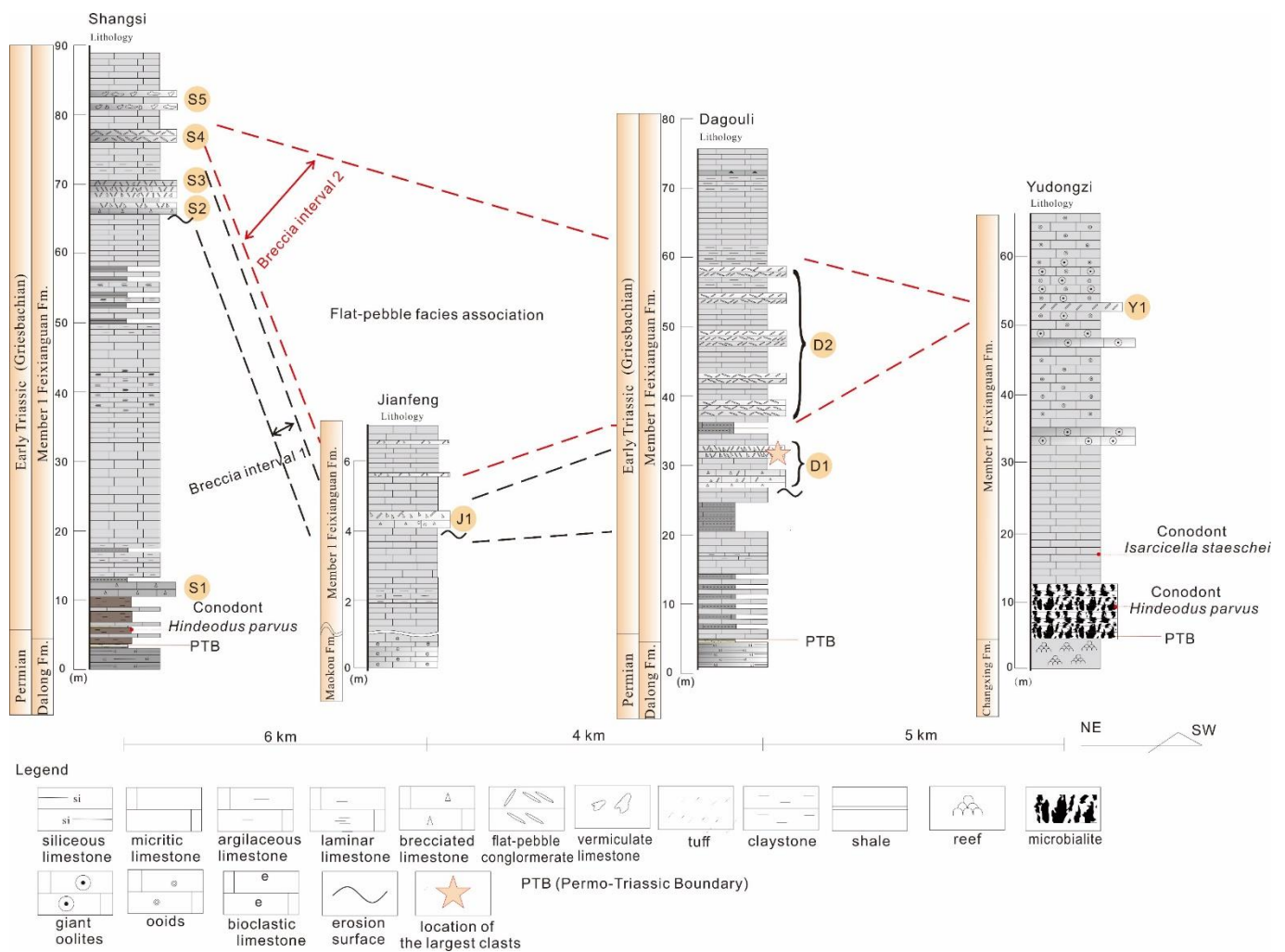


**Figure 2.** Stratigraphic logs of the sections exposing Member 1 of the Feixianguan Formation studied in this work and showing the event beds (S1–S5, D1–D2, J1, Y1). The PTB in the Shangsi Section is based on references [7], and the conodont stratigraphy is based on references [39]. The PTB in the Yudongzi Section is based on references [44], and its conodont stratigraphy is based on references [45].

### 3. Materials and Methods

The data for this study were collected at four stratigraphic sections located in the northwestern Sichuan Basin, namely, Shangsi, Dagouli, Jianfeng, and Yudongzi (Table 1). A total of 180 intraformational calcirudite rock samples were collected for observation and analysis using transmitted-light microscopy at the Institute of Sedimentary Geology, Chengdu University of Technology. For microfacies analysis, 40 calcirudite samples were specifically selected. One half of the surface of each thin section was dyed using alizarin red to identify carbonate minerals, following the method outlined by Dickson (1965) [48]. A detailed petrographic study of these high-energy event deposits was conducted at the State Key Laboratory of Oil and Gas Reservoir Geology and Exploitation, Chengdu University of Technology. Microfacies analyses were carried out using standard models [49]. The classification of high-energy event beds follows the frameworks provided by Dunham (1962) [50] and Wignall and Twitchett (1999) [7]. In Wignall’s 1999 study [7], Beds S2 and S3 (see Figure 2) were termed the ‘Shangsi Breccia Bed’ (SBB).

**Table 1.** Section location and sample distribution.

| Section Name   | Coordinates                 | Sample Location  | Total |
|--|-----------------------------|--|-------|
| Shangsi  | 105°28'13" E<br>32°18'30" N | Ten samples were collected at Bed S1 with a sampling interval of 10 cm; twenty-five samples were collected at Beds S2 and S3 with a sampling interval of 10 cm; ten samples were collected at Bed S4 with a sampling interval of 5 cm; ten samples were collected at Bed S5 with a sampling interval of 10 cm. | 55    |
| Jianfeng   | 105°21'41" E<br>32°17'23" N | Twenty samples were collected at Bed J1 with a sampling interval of 5 cm.  | 20    |
| Dagouli  | 105°16'49" E<br>32°17'35" N | Thirty samples were collected at Bed D1 with a sampling interval of 10 cm; fifty-five samples were collected at Bed D2 with a sampling interval of 10 cm.  | 85    |
| Yudongzi   | 105°06'08" E<br>32°02'35" N | Twenty samples were collected at Bed Y1 with a sampling interval of 5 cm.  | 20    |
| The positions of beds S1-S5, J1, D1, D2, Y1 are shown in Figure 2. |                             |  | 180   |

#### 4. Results

Intraformational calcirudites within Member 1 of the Feixianguan Formation are observed across consecutive sections at Shangsi, Dagouli, Jianfeng, and Yudongzi in the study area (Figure 3). In the lower part of Member 1 in the Shangsi section, a calcirudite layer is commonly embedded in marl. Meanwhile, the upper part is rich in breccias and flat-pebble conglomerates (Figures 2, 3A and 4). In the Dagouli section, abundant calcirudites appear to occur in the middle unit of Member 1 of the Feixianguan Formation, and mainly consist of flat-pebble conglomerates (Figures 2, 3B and 4). At Jianfeng, a calcirudite bed of approximately 20 cm in thickness is part of the limestone sequence (Figures 2, 3C and 4). By contrast, the calcirudites at Yudongzi are found within ooid limestones (Figures 2, 3D and 4). The sedimentary characteristics of Beds S2, S3, D1, and J1 resemble those of the ‘Shangsi Breccia Bed’, each featuring an erosional surface at the base. Additionally, Beds S4, Y2, and J1 consist of flat-pebble conglomerates (see Figure 2). These event deposit beds display lateral comparability (see Figure 2).

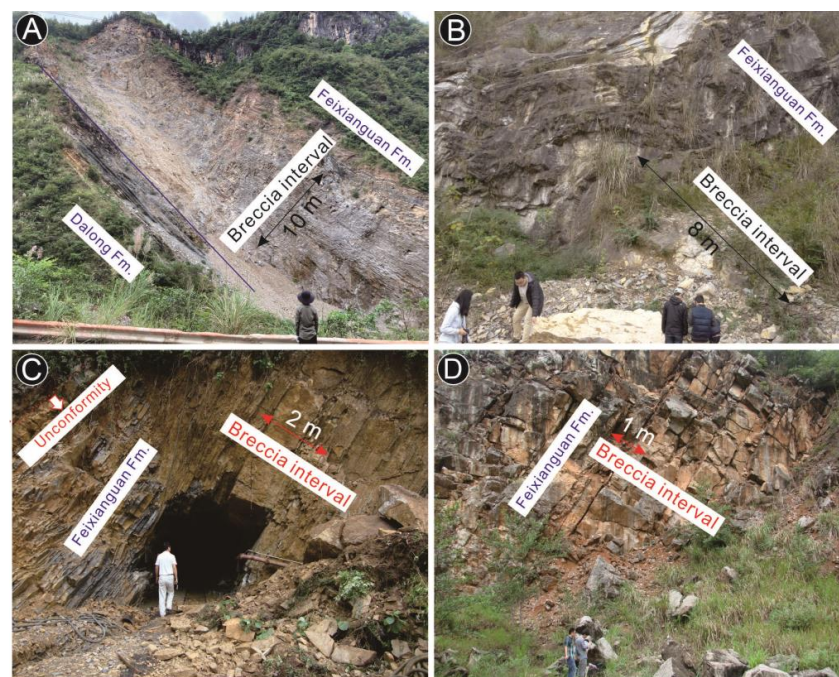


**Figure 3.** Photographs of the lower Feixianguan Formation from the NW Upper Yangtze Region. (A) Shangsi section. (B) Dagouli section. (C) Jianfeng section (white line for scale: 1 m). (D) Yudongzi section.

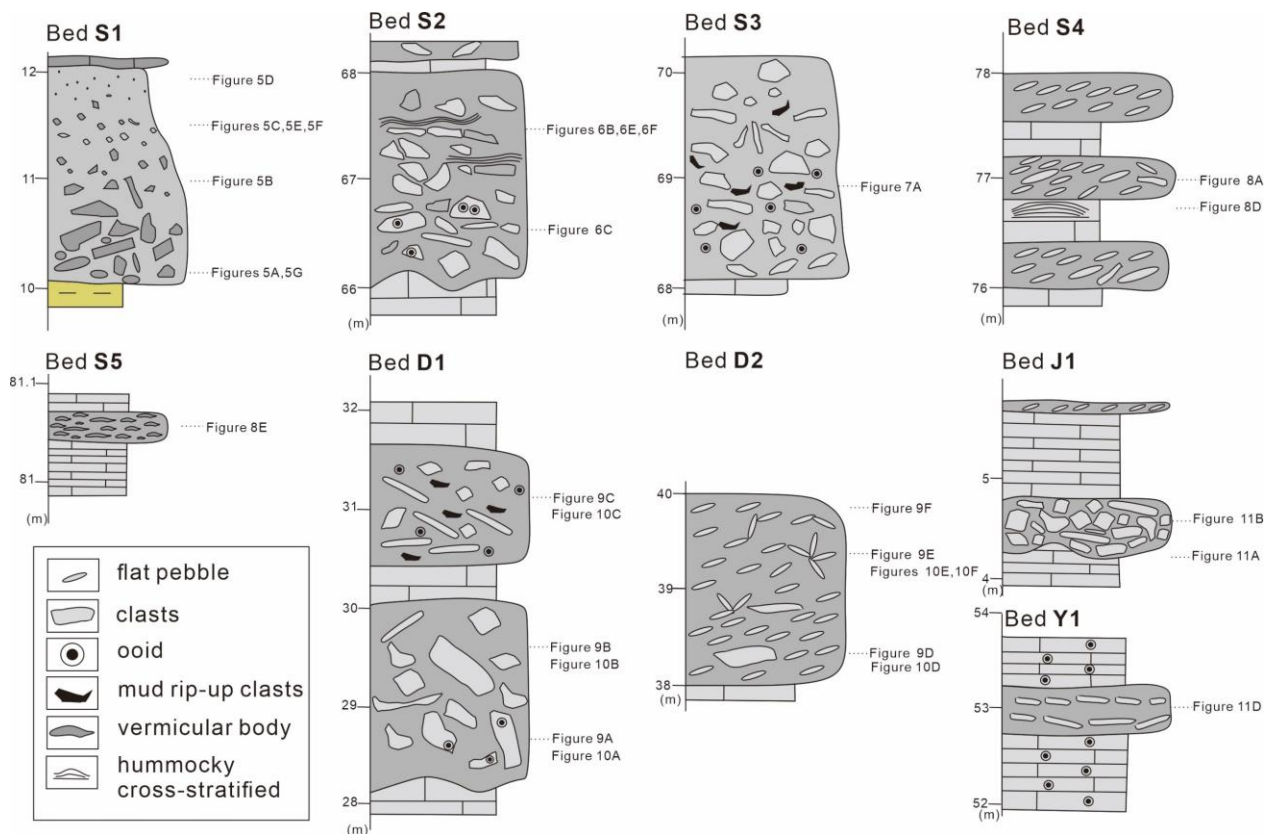


**Figure 4.** High-energy event beds from the studied section.

#### 4.1. Shangsi Section

Five event beds, designated S1–S5, have been identified in Member 1 of the Shangsi section (see Figures 2 and 4).

S1: this bed predominantly comprises grey calcirudites, which consist of intraclasts, a matrix, and a small quantity of flat pebbles. The gravel is dark gray, while the matrix is light gray (Figure 5). This bed varies from bottom to top in the content, shape, and distribution of intraclasts. Based on sedimentary characteristics, the calcirudites can be categorized into four types, as follows. (1) The intraclast content exceeds 50% and is supported by a matrix. The intraclasts are mostly thin plates and generally lie with their axes parallel to the bedding plane (Figure 5A). (2) The intraclast content ranges from 30 to 50%. This type displays normal grading and includes brittle clasts (Figure 5B). (3) The intraclast content is between 10 and 30%. The intraclasts are relatively short and distributed disorderly (Figure 5C). (4) The intraclast content is less than 10% and is matrix-supported. The clasts in this bed show little variation in size and are darker in color (Figure 5D). Under microscopic examination, the clasts are composed of grainstone and laminated packstone, while the matrix consists of micrite (Figure 5E–G). Bioclasts are rare in this bed.

S2: this bed, identified as the lower part of the Shangsi Breccia Bed (SBB) by Wignall (1999) [7], consists of grey intraclasts and calcirudites and contains flat pebbles (Figure 6). The clasts range in size from a few millimeters to 20 cm and are composed of wackestone, marl, and oolitic limestone (Figure 6C,D). Most tabular clasts (i.e., flat pebbles) have jagged borders (Figure 6E,F). Evidence of plastic deformation and reworking is present, with common structures including soft-sediment deformation and sutured contacts around intraclasts (Figure 6B,E,F).

S3: in this bed, identified as the upper part of the Shangsi Breccia Bed (SBB) by Wignall (1999) [7], the calcirudites consist of tabular intraclasts, mud rip-up clasts, ooids (or oolites), cortoids, and bioclasts (Figure 7). Most tabular intraclasts measure 5–20 cm along their axes (Figure 7A). The ooids, approximately 0.3–1 mm in diameter, are epidermal and oolitic with

concentric laminae (Figure 7C–F). Many are partially preserved and display evidence of pressure solution (Figure 7E). The ooid nuclei generally consist of sparry calcite (Figure 7F). Additionally, ostracod and microgastropod bioclasts are also found (Figure 7H,I).

S4: this event deposit comprises multiple beds of flat-pebble conglomerate, with the pebbles primarily consisting of marl (Figure 2). The long axis of the pebbles ranges from a few millimeters to 10 cm (Figure 8A,B). The conglomerates are commonly matrix-supported and contain approximately 50% pebbles (Figure 8A,C). Some pebbles are mostly subparallel to the bedding planes and occasionally exhibit imbrication, swirling, and a pressure solution fabric (Figure 8A,B). Some primary sedimentary structures, such as hummocky cross-stratification, are also present (Figure 8D).

S5: This bed, approximately 6 cm thick, is composed of vermicular limestone (Figure 8E). The vermicular limestone is matrix-supported (Figure 8F). The vermicular bodies are relatively irregular and primarily consist of micritic calcite; they are nearly homogeneous (Figure 8F). In this bed, algal laminae structures and suspected saccate microorganisms are observed in some instances, occasionally appearing as bioclasts (Figure 8G). Vermicular bodies are distributed throughout the entire bed, and their orientation varies from being parallel to the bedding to being random (Figure 8E).

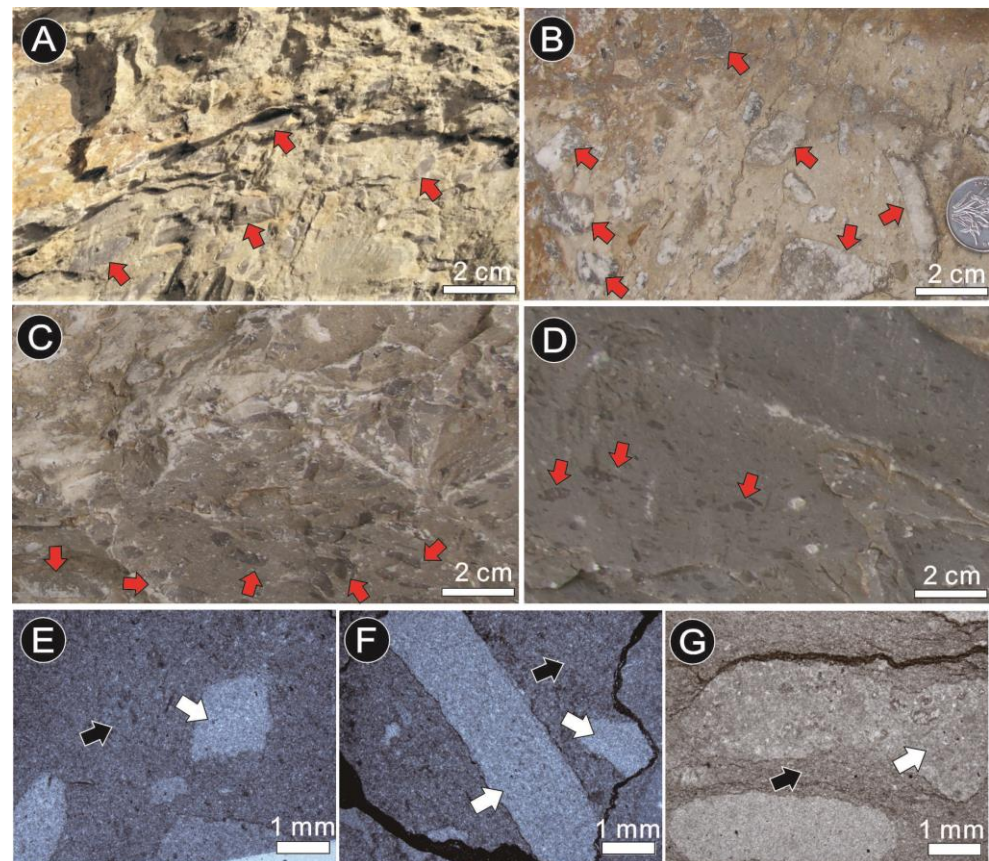


**Figure 5.** Photographs of calcirudites in Bed S1, taken both at the outcrop and under the microscope. (A) Calcirudites in the lower part of Bed S1; red arrows indicate intraclasts. (B) Calcirudites in the middle portion of Bed S1, showing normal grading; red arrows indicate intraclasts. (C,D) Calcirudites in the upper part of Bed S1, illustrating that the content of intraclasts gradually decreases upwards; red arrows indicate intraclasts. (E,F) Thin-section views of calcirudites in the upper part of Bed S1; red arrows indicate intraclasts and white arrows indicate the matrix. (G) Intraclasts in the lower part of Bed S1 are indicated by white arrows, and the matrix is indicated by black arrows.

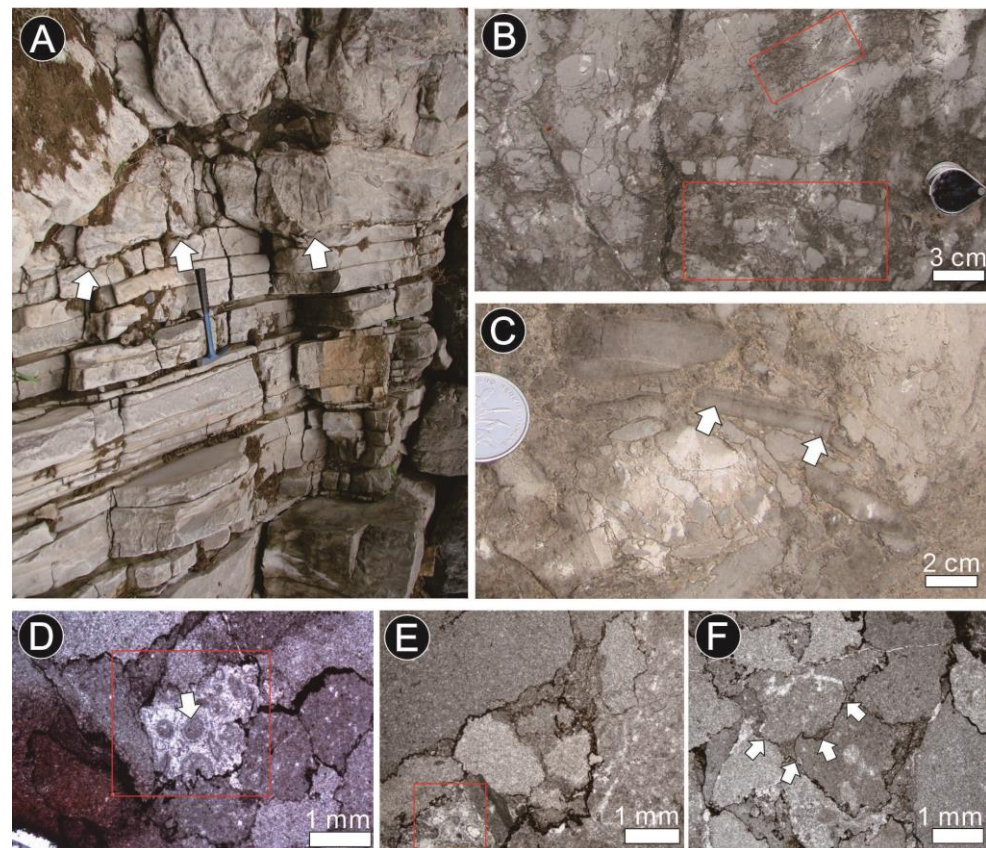


**Figure 6.** Photographs and microphotographs of calcirudites in Bed S2. (A) Calcirudites overlying thin-bedded marl with an erosional surface; white arrows indicate the bottom of the Shangsi Breccia Bed (SBB) (geological hammer for scale: 30 cm). (B) Soft-sediment deformation indicated by the red box. (C) Tabular clasts, indicated by white arrows, showing in situ progressive fragmentation. (D) Irregular clasts highlighted in red boxes, made of micrite and oolite, separated by stylolites; white arrows indicate oolite. (E) Micrite and bioclastic grains, highlighted in red boxes, vary in size; white bar for scale: 1 mm. (F) A well-developed stylolite structure along the margin of grains, indicated by white arrows.

#### 4.2. Dagouli Section

Based on the observations of sedimentary structures and lithological features exhibited in the calcirudite beds, the event beds at Dagouli can be classified into two main types: (1) brecciated limestones containing tabular clasts (D1), and (2) flat-pebble conglomerates (D2).

D1: bed D1 primarily consists of brecciated limestones, tabular intraclasts, and micrites (Figure 9A). The clasts' long axes range from a few millimeters to 30 cm. Light gray micrites and ooids are observed within these clasts (Figures 9B,C and 10A). The micrite clasts are either angular or subrounded in shape and are supported by a matrix. Many are highly tabular, with cross-sections reaching up to 1 cm (Figure 10B,C). The matrix is composed of clay minerals and microcrystalline calcite (Figure 9B). In the top layer of Bed D1, the clasts are smaller and display a normally graded bed sequence (Figure 9).

D2: at least five beds of flat-pebble conglomerate are observable in Bed D2. These event beds are commonly interbedded with micritic limestones. The flat pebbles are mostly subparallel to the bedding planes and occasionally exhibit a 'chrysanthemum structure' (Figure 9E). While some flat pebbles reach up to 20 cm in length, the majority range from 0.5 to 5 cm along their axis, making them larger than the flat pebbles found in Bed S3 (Figure 9D,F). Bed D2's flat-pebble conglomerate contains micrites, bioclastics, and pebbles (Figure 10D–F). The pebbles are generally oblate in shape with angular edges (Figure 10F) and are primarily composed of micrites. Additionally, bioclastics, such as

ostracods, tubeworms, foraminifera, and microgastropod fossils, are occasionally observed in D2 (Figure 10E). The matrix is comprised of pelmicrite, which structurally corresponds to the micritic pebbles (Figure 10D,F).

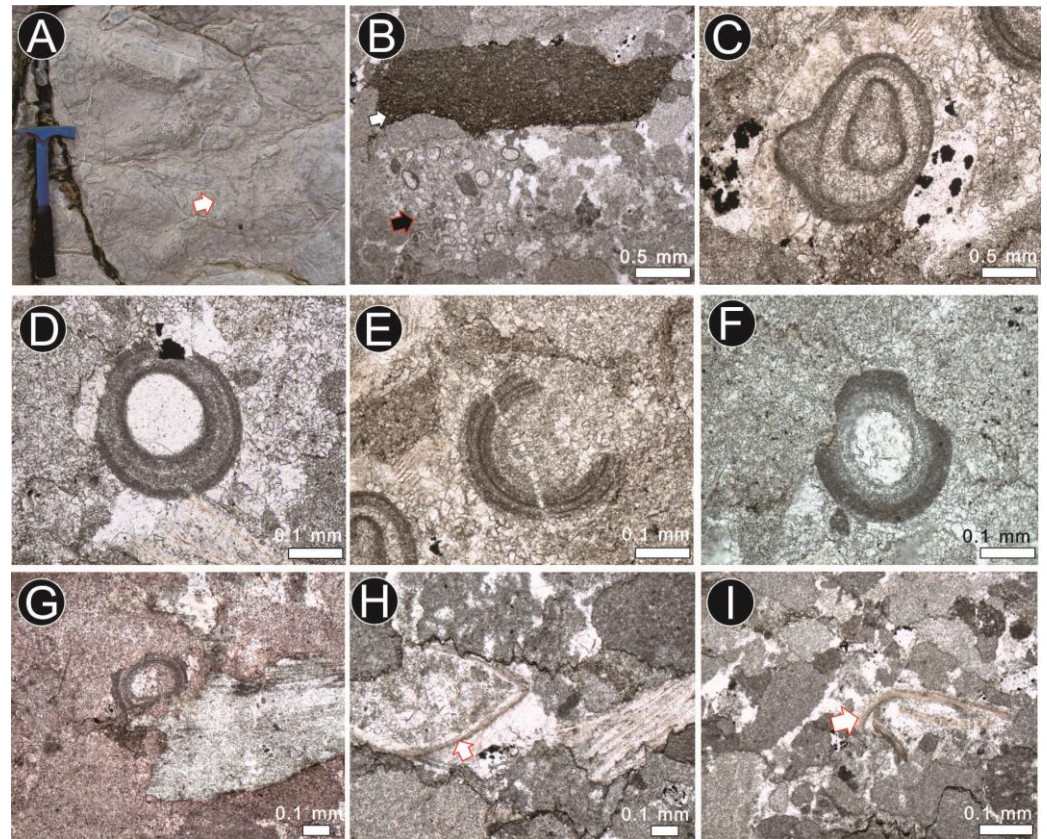


**Figure 7.** Photographs and microphotographs of calcirudites in Bed S3. (A) Tabular intraclasts, indicated by white arrows, are randomly orientated (geological hammer for scale: 30 cm). (B) Rip-up mudstone and oolitic clasts, indicated by white and black arrows, respectively. (C) Cortoids. (D–G) Ooids. (H) Microgastropod fossils, indicated by white arrows. (I) Ostracod and microgastropod fossils, indicated by white arrows.

#### 4.3. Jianfeng Section

The event bed, which is characterized by calcirudites and intraclasts (Figure 11A), overlies the thin-bedded limestones found at the lowest part of the Triassic layer. It is situated above an erosive unconformity that separates the Permian Dalong Formation from the Triassic Feixianguan Formation. This grey bed, designated as J1 in this study, exhibits a variable thickness ranging from 1 to 1.5 m (Figure 11B). The clasts in this bed consist of grainstones and micrite limestone and display normally graded bedding (Figure 11C). The size of the clasts varies from a few millimeters to 3 cm along their long axis, and the rock is predominantly grain-supported. The clasts are generally irregular in sphericity and occasionally exhibit elongation. Compared to the brecciated limestone found in Shangsi, the matrix of this bed has a lower argillaceous material content.

#### 4.4. Yudongzi Section

The event beds in the Yudongzi section are primarily composed of flat-pebble conglomerates (Y1) (Figure 11D). These flat-pebble conglomerates are predominantly composed of angular clasts that have tabular shapes (Figure 11D). The clasts, also known as flat pebbles, are composed of micrites and oolites (Figure 11F) and range from a few millimeters to 5 cm along their long axis. The conglomerate is primarily matrix-supported. The flat pebbles are primarily orientated subparallel to the bedding plane, although some are randomly

dispersed. The matrix exhibits both sparry cementation and occasional dolomitization, as shown in (Figure 11E).

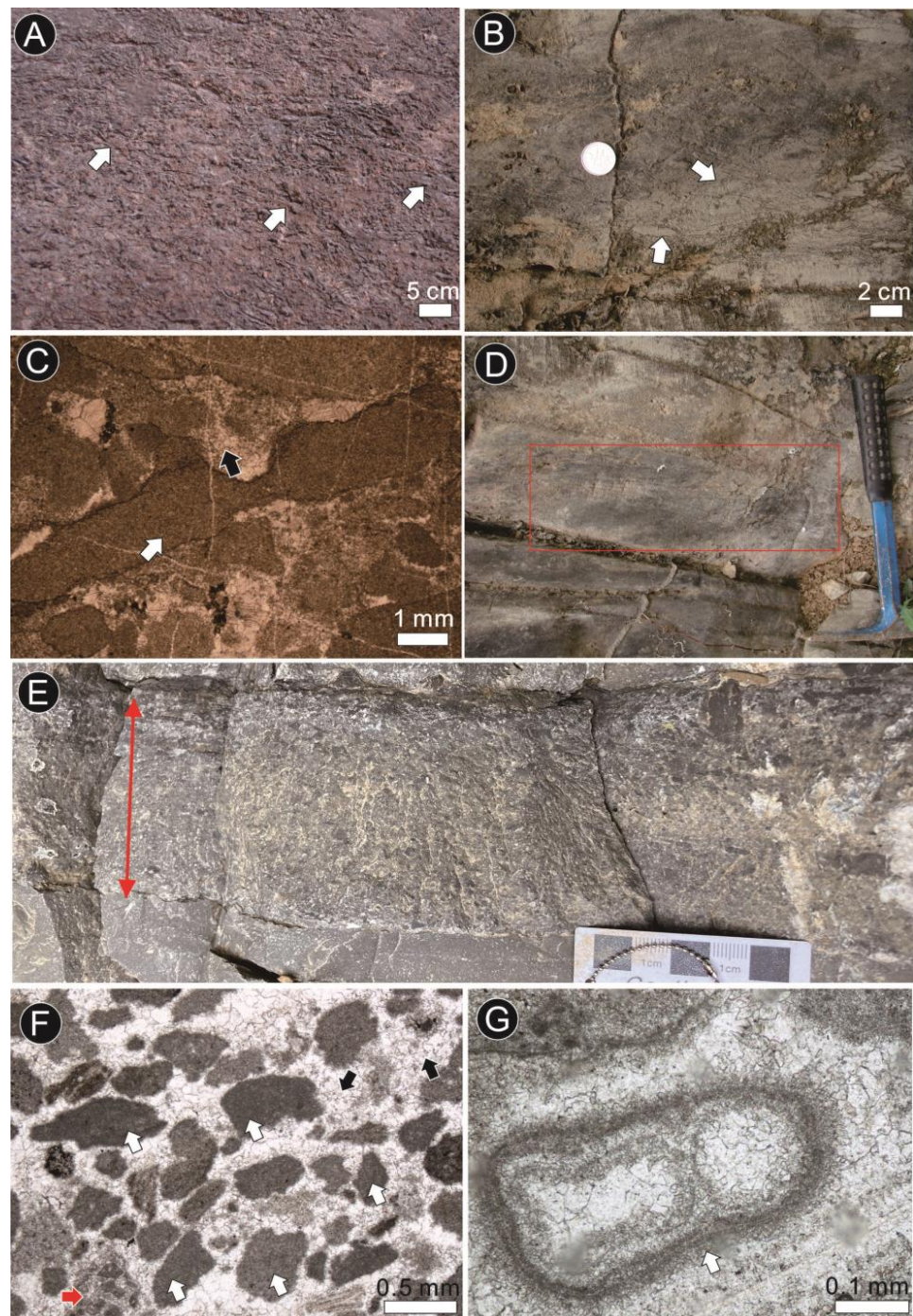


**Figure 8.** Outcrop photographs and microphotographs of calcirudites in Bed S4 (A–D) and S5 (E–G). (A) A flat-pebble conglomerate showing swirling and randomly arranged grainstone clasts; white arrows indicate the flat pebbles. (B) A flat-pebble conglomerate; white arrows indicate the flat pebbles. (C) The microscopic characteristics of the flat-pebble conglomerate; white arrows indicate the flat pebbles, and black arrows indicate the matrix. (D) Hummocky cross-bedding is visible; white arrows indicate the structure (geological hammer for scale: 30 cm). (E) A vermicular limestone bed; red arrows indicate the feature. (F) An algae laminae structure, suspected saccate microorganisms, and micritic calcite are visible; white, red, and black arrows indicate these features, respectively. (G) A possible saccate microorganism.

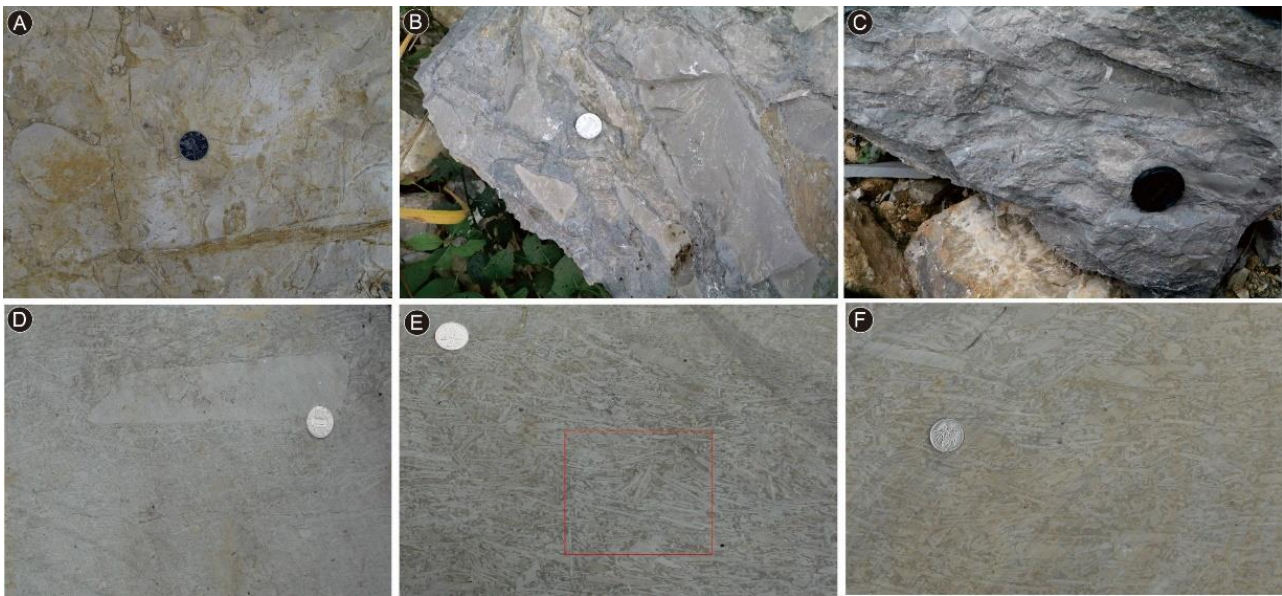


**Figure 9.** Photographs of Beds D1 (A–C) and D2 (D–F) captured on both the outcrop and microscopic scales. (A) Brecciated limestones in Bed D1 (coin for scale: 1.9 cm). (B) Large, tabular intraclasts in Bed D1 (coin for scale: 1.9 cm). (C) Additional tabular intraclasts in Bed D1 (coin for scale: 1.9 cm). (D) A flat-pebble conglomerate found in Bed D2 (coin for scale: 1.9 cm). (E) A chrysanthemum structure in Bed D2, highlighted within the red square frame (coin for scale: 1.9 cm). (F) Flat pebbles in Bed D2 with predominantly horizontal orientations (coin for scale: 1.9 cm).

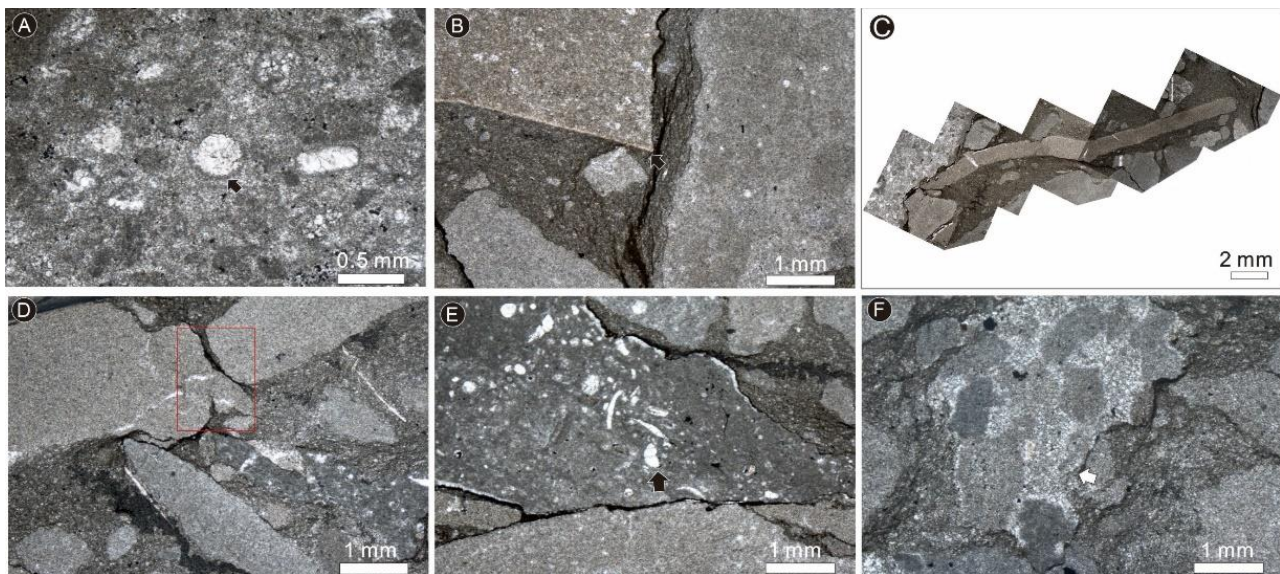


**Figure 10.** Photographs of Bed D1 (A–C) and D2 (D–F). (A) The microscopic characteristics of Bed D1, ooids (black arrow). (B) Angular clasts (black arrow) and argillaceous matrix. (C) Tabular intraclasts in a cross-section. (D) The microscopic characteristics of Bed D2, splivable clasts (in the red square frame). (E) Bioclastics in pebble, microgastropods (black arrow). (F) recycled pebbles, original pebble (white arrow).

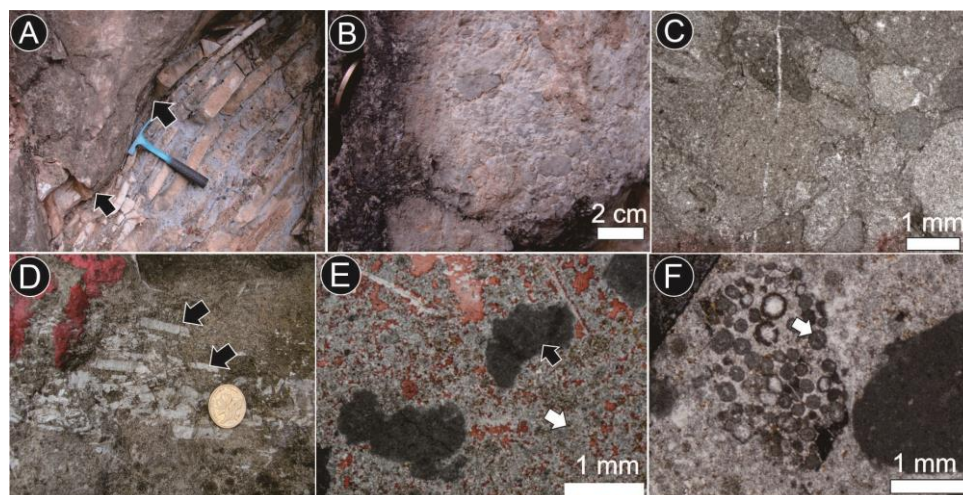


**Figure 11.** Photographs of calcirudites in Beds J1 (A–C) and Y1 (D–F), both at the outcrop and under a microscope. (A) Calcirudites overlaid by thin marl, with an erosional surface indicated by a black arrow; observed in overturned beds (geological hammer for scale: 30 cm). (B) Close-up view of calcirudites. (C) The microscopic characteristics of Bed J1. (D) Flat-pebble conglomerate. (E) Mud rip-up clasts indicated by a black arrow, and dolomitization indicated by a white arrow. (F) Oolitic limestone intraclasts highlighted by a white arrow.

## 5. Discussion

### 5.1. A Comparison of the Studied Outcrops

In this study, four sections are examined, and their stratigraphic correlations are systematically described. As a candidate for the Global Stratotype Section and Point (GSSP) of the Permian–Triassic Boundary (PTB), the Shangsi section features a continuous succession of deeper-water facies [7]. Studies on biostratigraphy, sedimentology, geochemistry, and geochronology have been conducted at Shangsi [32,39]. Bed 27, primarily composed of claystone, has been identified as marking the mass extinction boundary [32]. The claystone layer in the Dagouli section, along with the unconformable interface between the Dalong and Feixianguan Formations, is regarded as a lithologic boundary for the Permian–Triassic transition. This boundary, however, is not documented in the Jianfeng Section. Additionally, aside from the deep-water sedimentary profile, the lithologic boundary for the Permian–Triassic transition in the Yudongzi Section is primarily composed of microbialite. In summary, although the lithological assemblages of the PTB are diverse in the study area, the PTB in these profiles is clearly identifiable.

### 5.2. Assessing the Diagenetic Effects for Member 1 of the Feixianguan Formation

As a stage in rock formation, diagenesis has the potential not only to induce the erosion and alteration of the original sediment but also to modify the primary sedimentological signal [51]. Several major types of diagenetic effects have been previously identified, including compaction, pressure solution, dissolution, reprecipitation, and metasomatism. [51]. Careful petrographic observations in the study section reveal that Member 1 of the Feixianguan Formation contains potential diagenetic products including limestone–marl sequences, stylolite structure, and fragmentary ooids.

Munnecke et al. (2023) [52] proposed that limestone–marl sequences undergo a differential diagenesis during the burial stages. These diagenetic processes, such as dissolution, ion migration, and reprecipitation, result in the redistribution of calcium carbonate from marl layers to limestone beds. The limestone–marl alternations described here consist of tightly cemented limestone beds alternating with less resistant, less cemented marl beds (see limestone–marl alternations in Figures 2 and 3A). We interpret the lack of compaction in the limestone beds as evidence of early diagenetic cementation.

The prevailing view holds that stylolite structures are the result of a pressure solution [53]. Our study conclusively shows that certain clasts display a stylolite texture (Figure 6F). The concavo-convex contacts between these clasts indicate that they were well compacted, likely due to a shallow burial (Figure 6). In addition, Bed S3 described here contains some fragmented ooids in the matrix. The edges of these ooids exhibit pressure-solution structures (Figure 7F). The presence of these potential diagenetic products suggests that diagenetic alterations have broadly impacted Member 1 of the Feixianguan Formation. Although diagenesis has altered the high-energy event beds, the brecciation that produced these clasts is more likely the result of sedimentary processes [8].

### 5.3. Potential High-Energy Events

Griesbachian flat-pebble conglomerates are distinguished by their subangular pebbles and basal erosional surfaces, and the general orientation of the long pebble axes parallel to the bedding [7]. In certain studies, these macroscopic features are frequently seen as evidence of intense storm erosion and alteration [12,54]. However, the erosional surface may not necessarily be the result of subaerial exposure. Abdolmaleki and Tavakoli (2016) [6] attributed it to chemical factors, such as undersaturation conditions, along with a physical factor—namely, high-energy currents. Some breccia and flat pebbles in Beds S2, S3, and D1 are noticeably larger in size, suggesting an enigmatic underlying cause [7]. This latter evidence suggests that some catastrophic event, such as a tsunami, may be behind their deposition. In contrast, smaller flat pebbles could also result from less energetic events, such as storms.

#### 5.3.1. Seismic Event and Tsunami

A series of event clues are reported in the existing literature. For example, the presence of seismites (e.g., soft deformations, autoclastic breccias) in the Yangtze Block suggests that a series of seismic events played a significant role in Early Triassic deposition, following the turbulence in the Paleo-Tethys Ocean after the LPME [21,22]. Syndepositional deformations and calcirudites may be generated by earthquakes, based on numerous studies of seismites [55–61]. In the Yangtze Region, widespread Lower Triassic calcirudites are not exclusively triggered by seismic events [5]. Earthquake-induced tsunamis could also be responsible for the formation of flat-pebble conglomerates on both the local and regional scales [56,57]. Recent studies have categorized massive event sediments as tsunami deposits, which generally extend vertically for less than 25 cm but can span laterally for hundreds of meters [58]. These tsunami deposits found across the coastal zone often include rip-up clasts, indicating that most tsunami sediments are primarily in suspension [58]. Mud rip-up clasts are commonly found in the lower part of tsunami deposits in onshore areas [59]. In contrast, coarse sediments, mud clasts, and giant hummocky cross-stratification are typical features of tsunamites formed in shallow seas or on continental shelves [60–62]. If the energy of tsunami waves is very high, an erosional surface will result in such environments [61]. These sedimentary characteristics closely resemble those observed in Beds S2 and S3 at Shangsi (Figures 4–8), suggesting that tsunamis could be the primary triggering mechanisms for some of the calcirudites in the study area. Furthermore, the size of the clasts and the ability to correlate Bed D1 across the studied sections suggest that its origin may be linked to a large, regional tsunami (Figure 9B).

The primary causes of tsunamis encompass earthquakes, submarine sediment collapses, volcanic eruptions, and asteroid impacts [62]. Frequent earthquakes and volcanic activities during the Early Triassic period may have played a role in the generation of tsunamis [63–65]. For instance, at Shangsi, the large-scale soft deformations (syndepositional crinkled deformation) observed in Member 1 of the Feixianguan Formation beneath the SBB are interpreted as evidence of an earthquake [66]. Furthermore, evidence of potential asteroid impacts has been documented in PTB and Lower Triassic sequences at various locations worldwide [67,68], such as the Araguainha meteorite impact [69]. Additional evidence, including extraterrestrial noble gases in fullerenes from Japan [70], melt rocks

and impact breccias from Australia [71], and meteorite fragments from Antarctica [72], has also been reported. However, the exact chronology of these events remains uncertain. Koeberl et al. (2004) [73] argued against the idea that extraterrestrial events triggered the LPME. Therefore, the formation mechanism of tsunamis during this period is complex, and this study does not offer additional evidence.

### 5.3.2. Storms

Storm-dominated sequences are often observed in the Lower Triassic [74,75]. The evidence supporting this includes hummocky cross-stratification and tempestites, which suggest extreme climate conditions [75,76]. Current meteorological studies indicate that extreme storms typically originate from weak tropical vortices [77]. When the ocean surface temperature reaches 26.5 °C at a depth of 60 m, tropical cyclones gradually evolve into storms [78]. In comparison, the mass extinction at the Permian–Triassic boundary was likely caused by extreme warming events [79,80]. During the recovery period following this extinction, the global climate was extremely hot [80,81]. The development of an extremely warm climate led to a significant increase in sea-surface temperatures (SSTs) during the early Triassic [19], likely intensifying the frequency and intensity of hurricanes [79]. Furthermore, the equatorial symmetry of Pangaea during the Early Triassic might have led to the dominance of megamonsoons [82], thereby enhancing storm currents [27]. In this study, we identified a ‘chrysanthemum structure’ in the flat-pebble conglomerate at Bed D2 and hummocky cross-stratification at Bed S4, both of which may reflect the influence of storms [83]. Similar Lower Triassic storm records have also been found in the mid-Tethys realm [17].

### 5.4. Origin of High-Energy Event Deposits

Previous studies have proposed both sedimentary and diagenetic mechanisms for the formation of flat-pebble conglomerates. The former refers to the formation of semi-consolidated or consolidated thin-bedded carbonate rocks in a shallow-water marine environment [84]. These carbonate beds were broken, worn, transported, and accumulated under the influence of strong currents, tides, or storms [7,10,85]. As for the diagenetic origin, it is interpreted that intraclasts form through compaction and dehydration [86]. These autoconglomerates were compacted and crushed during the diagenetic period, as evidenced by uniform pebble clasts in their composition, argillaceous matrix, crack structures, and ‘boudin’ structures [87]. However, the flat-pebble conglomerates in this study do not show evidence of compaction or any of the forementioned structures, making it unlikely that they were formed in diagenesis. Furthermore, the flat-pebble conglomerates during the Early Triassic are commonly regarded as ‘anachronistic facies’ when interpreting environmental conditions after the LPME, which oversimplifies both their origin and their environmental interpretation [88]. Here, we provide a detailed analysis of the formation of Early Triassic event beds in the Upper Yangtze Region.

In this study, we found that the clasts in brecciated limestones and flat-pebble conglomerate are composed of micritic calcite, silty calcite, prior calcirudite, and oolitic limestone. These clasts originate from laminated microcrystalline limestone, argillaceous limestone, and oolitic limestone beneath the event beds. Although the Lower Triassic laminated microcrystalline limestone was previously interpreted as having been deposited under environmental conditions such as low energy, anoxia, and a stagnation of the ocean cycle [89], it would be incorrect to assume that such low-energy environmental conditions persisted until the deposition of Beds S2, D1, J1, and Y1. The presence of recycled pebbles in Bed D2 suggests a gradual transition from a low-energy to high-energy environment. Paleoclimate studies of the Early Triassic suggest that a decrease in trade winds, caused by the weakening of the Hadley cell in response to greenhouse-induced warming, led to prevailing hypoxic conditions in the Paleo-Tethys, resulting in nearly stagnant ocean currents [90].

In the study area, ooids can be found in the calcirudite (Beds S3, D1) (Figures 7 and 8). Oolites were documented in the Lower Triassic carbonate platform facies in the Yudongzi Section (Figure 2), suggesting that some of the ooids in Beds S3 or D1 originated from a nearshore environment, such as that at Yudongzi. The oolitic types and characteristics of S3 and D2 are similar to those of the Yudongzi section. The input of ooids into offshore regions (e.g., at Shangsi) was probably triggered by the backflow of tsunamis (Figure 1), resulting in both oolite breccia and individual ooid grains being deposited in the calcirudite bed. Although ooids were widespread in shallow marine carbonate settings during the Early Triassic recovery interval [91], the diversity of clast compositions indicates that the material source of the event beds is regional in the study area.

Flat pebbles and breccia are often considered to be carbonate intraclasts of a similar origin [84]. These intraclasts are usually considered to be redeposited in situ or near the source in sedimentary basins [49]. Despite their importance, the transport distance of intraclasts has hardly been studied. In fact, the transport distance could reveal the nature, size, and frequency of geological events or the triggering mechanism [56,92]. In the studied event beds, limestone gravels are subrounded, and the flat pebble conglomerate commonly has a matrix-supported structure (Figures 5–11). These characteristics suggest that the transport distance of the gravels was relatively short. Referring to the slope setting of the study area [30], storm waves and gravity are the main driving forces behind this transport. The transport medium could be a debris flow [24], tractive current, or eddy current. Moreover, a rapid diagenesis of event sediments occurred during deposition. Factors such as the upwelling of alkaline and anoxic deep waters, high rates of evaporation, extremely high temperatures, and the global sea-level rise in the Early Triassic marine environment also contributed to this diagenesis [9].

### 5.5. Depositional Model

The event succession at the northwestern margin of the Sichuan Basin was deposited on a platform margin slope during the Early Triassic [93]. Based on the microfacies characteristics of event beds from four outcrop sections—Shangsi, Dagouli, Jianfeng, and Yudongzi (Figure 2)—it is evident that at least three high-energy events were recorded during the Griesbachian period (i.e., the deposition of Member 1 of the Feixianguan Formation) (Figure 12).

In the lower part of Member 1 of the Feixianguan Formation (Bed S1), calcirudite indicates the presence of a submarine debris flow during the early Griesbachian (Figure 12A). Carbonate slope environments are essential for gravity flow [94]. Such a gravity flow was present along the platform margin of the Early Triassic Kaijiang–Liangping Bay in the Upper Yangtze Block [95]. Intense tectonic activity has been proposed as an explanation for the origin of gravity flow in the study area [24]. In Bed S1, the rock is matrix-supported and contains normal-grained gravel debris, tabular gravel debris, and a plain bed plane at the bottom of the limestone (Figure 6). These features suggest a rapid collapse of detrital material. Due to an unrevealed triggering mechanism, the clastic material formed a debris flow that moved steadily along the slope. The scale and aftermath of this event were relatively restricted because Bed S1 is only found deposited at Shangsi.

Breccia limestone and calcirudite beds (Beds S2, S3, D1, J1) have the potential to be tsunamites. The size of the clasts in Beds S2 and D1, which are about tens of centimeters in size, suggests that they were formed by highly energetic events, such as tsunami waves. However, the plate-shaped, edge-smoothed clasts in Bed S3 indicate that high-energy currents have affected the breccia on multiple occasions. The possible tsunamigenic origin of the Shangsi Breccia Bed (SBB) (Beds S2, S3, D1, and J1) is supported by sedimentological characteristics, such as erosion surfaces, coarse sediments, and mud clasts (Figures 6–9). The mud rip-up clasts, ooids, and bioclasts in Bed S3 may indicate the backwash waters of a tsunami shortly following high-energy events, such as earthquakes or asteroid impacts (Figure 6). This interpretation is consistent with the common occurrence of mud rip-up clasts in modern tsunami deposits [58,61]. The oolites present in the Yudongzi section [45]

suggest that the ooids found in Beds S3 and D1 were transported from the Yudongzi area via tsunami return flow (Figure 12B). The bioclasts (Figures 7H and 10E) may have been transported from shallow water carbonate platforms via tsunami return flows.

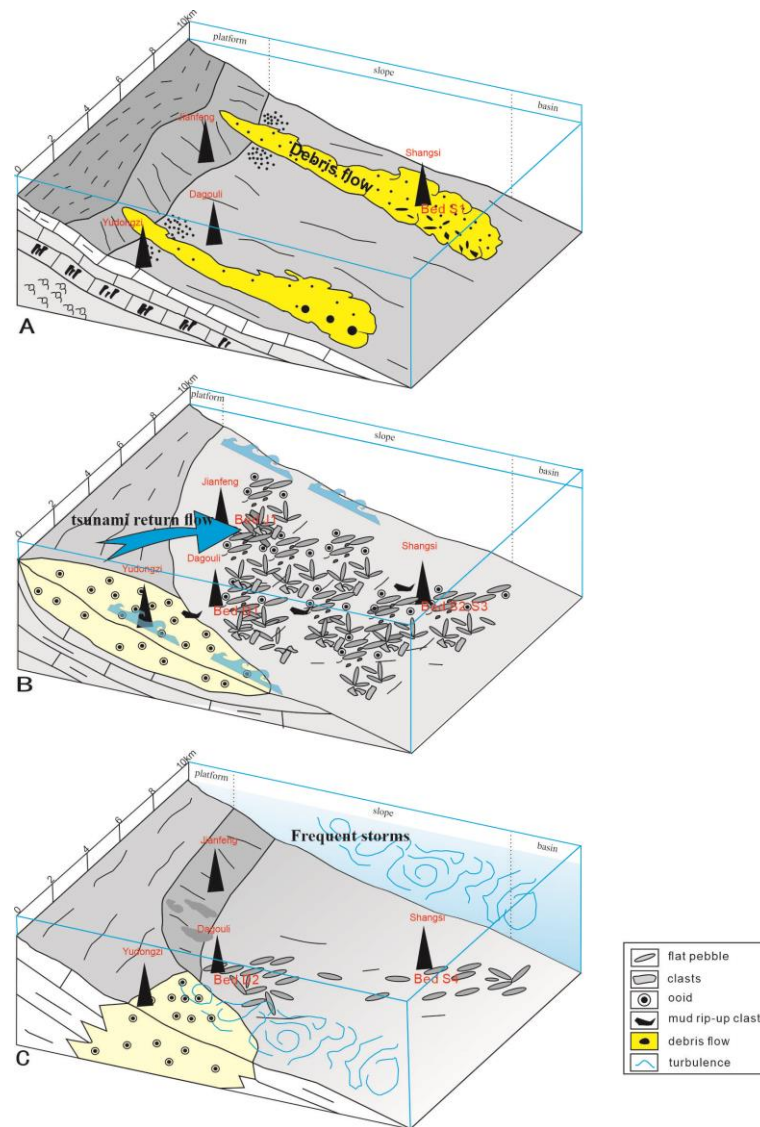


**Figure 12.** Diagram showing the high-energy event deposits during the deposition of Member 1 of the Feixianguan Formation. (A) Gravity flow: the scale of this event was restricted to the deep-water, lower-slope facies. (B) Megatsunami: the scale of the sedimentary response to this event was confined to the relatively shallow slope facies. (C) Frequent storms: the scale of the sedimentary response to this event developed across both the platform and slope facies.

Several flat-pebble conglomerate beds (Beds S4, D2, and Y1) demonstrate that deposition during the late Griesbachian was influenced by frequent storm events (Figure 12C). Key sedimentary structures indicative of storm deposits, such as hummocky cross-stratified and a ‘chrysanthemum-shaped’ arrangement of pebbles, are commonly observed in Beds S4 and D2 (Figure 8B). The brittle deformation of pebbles, likely due to clast–clast interactions (Figure 10D), may have been induced by these storms. In contemporary marine environments, extremely severe storms can produce similar sedimentary records, even though storms are more common at low latitudes [58]. It should be noted that these flat-pebble conglomerates were deposited after the tsunami event, implying that high-energy events might have led to long-term climatic anomalies and frequent storms during this stage.

The uppermost bed of the Griesbachian event deposit at Shangsi (Bed S5) features vermicular limestone (Figure 8E). The origin of Lower Triassic vermicular limestone is closely associated with specific marine chemical conditions. Following deposition, the mud (including vermiculate bodies) underwent syndimentary diagenesis and was influenced by macroorganism activity. Woods (2014) [8] also proposed that both biotic processes and harsh environmental conditions dictate the formation of vermicular limestone. In shallow-water environments, the occurrence of vermicular limestone seems to be unrelated to actualistic sedimentologic processes [8]. In this study area, the presence of vermicular limestone suggests that harsh marine conditions persisted after the frequent storm events that characterized the Early Triassic.

## 6. Conclusions

Through careful microfacies analysis of calcirudite beds from Shangsi and the surrounding sections, we elucidate the origins of the enigmatic intraclasts found at Shangsi. This study provides detailed characteristics and proposes a sequence concerning high-energy events in the Griesbachian (Early Triassic) calcirudites of Member 1 of the Feixianguan Formation, located at the northwest margin of the Yangtze Block.

At Shangsi, Dagouli, Jianfeng, and Yudongzi, at least ten event beds (S1–S5, D1–D2, J1, and Y1) have been identified. Bed S1 primarily consists of calcirudites and is interpreted as debris from flow deposits. Beds S2, S3, D1, and J1 contain evidence of tsunami backwash, including an erosional surface, mud rip-up clasts, ooids, and bioclasts, pointing to the occurrence of a tsunami event. Beds S4, D2, and Y1 comprise flat-pebble conglomerates, which contain features indicative of storm events, including the ‘chrysanthemum structure’, hummocky cross-stratification, and normally graded bed sequences. These attributes indicate frequent storm events during the Griesbachian. Bed S5 is predominantly made up of vermicular limestones, indicating that the marine environment in the Upper Yangtze Region remained inhospitable even after experiencing frequent high-energy events in the Early Triassic.

The findings of this study provide a valuable depositional model that illustrates high-energy events during the Griesbachian. The presence of debris flow deposits shortly after the PTB suggests intense tectonic activity in the study area during the earliest Early Triassic. Subsequent layers of breccia limestone suggest that the basinal water in the study area during the Early Triassic was high-energy, pointing to the potential occurrence of a massive tsunami. Additionally, sedimentary analysis reveals a link between flat-pebble conglomerate beds and frequent storm events. These various high-energy events in the study area likely contributed to the brecciation of different intraformational calcirudites. Therefore, Member 1 of the Feixianguan Formation in northwestern Sichuan encompasses a sequence that includes high-energy events such as gravity flows, tsunamis, and storms.

**Author Contributions:** Conceptualization, D.Q. and Z.S.; methodology, Z.S.; investigation, D.Q., Z.S. and X.D.; resources, Z.S.; writing—original draft preparation, D.Q.; writing—review and editing, Z.S. and X.D.; visualization, D.Q.; supervision, Z.S. All authors have read and agreed to the published version of the manuscript.

**Funding:** This study is funded by the Department of Science and Technology of Sichuan Province, China (Grant No. 2021YJ0353) and Natural Science Foundation (Grant No. 41572085) of the Chinese Ministry of Science and Technology.

**Data Availability Statement:** Field geological record data can be provided upon request to the corresponding author. The data are not publicly available due to privacy.

**Acknowledgments:** We thank Yixing Du, Xiang Zhang, and Yu Ge from Chengdu University of Technology, and Leopold Krystyn at Vienna University (Austria) for their assistance with the field work. We also appreciate the constructive suggestions from the editors and reviewers.

**Conflicts of Interest:** The authors declare no conflict of interest.

## References

1. Erwin, D.H. The Permo-Triassic extinction. *Nature* **1994**, *367*, 231–236.
2. Tong, J.N.; Lin, Q.X.; Shi, G.R. Evolution of the Permian and Triassic reef ecosystems in South China. *Proc. Royal. Soc. Victoria* **1998**, *110*, 385–399.
3. Racki, G. Silica-secreting biota and mass extinctions: Survival patterns and processes. *Palaeogeogra. Palaeoclimatol. Palaeoecol.* **1999**, *154*, 107–132. [[CrossRef](#)]
4. Retallack, G.J.; Veevers, J.J.; Morante, R. Global coal gap between Permian-Triassic extinction and Middle Triassic recovery of peat-forming plants. *GSA Bull.* **1996**, *108*, 195–207. [[CrossRef](#)]
5. Fraiser, M.L.; Bottjer, D.J. Restructuring of benthic level-bottom shallow marine communities due to prolonged environmental stress during the aftermath of the end-Permian mass extinction. *C. R. Palevol.* **2005**, *4*, 15–23. [[CrossRef](#)]
6. Abdolmaleki, J.; Tavakoli, V. Anachronistic facies in the early Triassic successions of the Persian Gulf and its palaeoenvironmental reconstruction. *Palaeogeogra. Palaeoclimatol. Palaeoecol.* **2016**, *446*, 213–224. [[CrossRef](#)]
7. Wignall, P.B.; Twitchett, R.J. Unusual intraclastic limestones in Lower Triassic carbonates and their bearing on the aftermath of the end-Permian mass extinction. *Sedimentology* **1999**, *46*, 303–316. [[CrossRef](#)]
8. Woods, A.D. Assessing Early Triassic paleoceanographic conditions via unusual sedimentary fabrics and features. *Earth Sci. Rev.* **2014**, *137*, 6–18. [[CrossRef](#)]
9. Zhao, X.M.; Tong, J.N.; Yao, H.Z.; Zhang, K.X.; Chen, Z.Q. Anachronistic facies in the Lower Triassic of South China and their implications to the ecosystems during the recovery time. *Sci. Chin. Ser. D Earth Sci.* **2008**, *51*, 1646–1657. [[CrossRef](#)]
10. Woods, A.D. Microbial ooids and cortoids from the Lower Triassic (Spathian) Virgin Limestone, Nevada, USA: Evidence for an Early Triassic microbial bloom in shallow depositional environments. *Glob. Planet Chang.* **2013**, *105*, 91–101. [[CrossRef](#)]
11. Deng, B.Z.; Wang, Y.B.; Woods, A.D.; Li, S.; Li, G.S.; Chen, W.H. Evidence for rapid precipitation of calcium carbonate in South China at the beginning of Early Triassic. *Palaeogeogra. Palaeoclimatol. Palaeoecol.* **2017**, *474*, 187–197. [[CrossRef](#)]
12. Pruss, S.B.; Corsetti, F.A.; Bottjer, D.J. The unusual sedimentary rock record of the Early Triassic: A case study from the southwestern United States. *Palaeogeogra. Palaeoclimatol. Palaeoecol.* **2005**, *222*, 33–52. [[CrossRef](#)]
13. Woods, A.D.; Alms, P.D.; Monarrez, P.M.; Mata, S. The interaction of recovery and environmental conditions: An analysis of the outer shelf edge of western North America during the early Triassic. *Palaeogeogra. Palaeoclimatol. Palaeoecol.* **2019**, *513*, 52–64. [[CrossRef](#)]
14. Chen, L.Z.; Luo, X.M.; Xiao, J.D. Early Triassic calcareous storm deposits in southeastern Hubei. *Sediment. Fac. Palaeogeogra.* **1991**, *11*, 1–9. (In Chinese with English abstract)
15. Collinson, J.W.; Kendall, C.G.S.C.; Marcantel, J.B. Permian-Triassic boundary in eastern Nevada and west-central Utah. *Geol. Soc. Am. Bull.* **1976**, *5*, 821–824. [[CrossRef](#)]
16. Alvarez, W.O.; Connor, D.; Koeberl, C. Permian-Triassic boundary in the southwestern United States: Hiatus or continuity? In *Catastrophic Events and Mass Extinctions: Impacts and Beyond*; Koeberl, C., MacLeod, K.G., Eds.; Geological Society of America: Boulder, CO, USA, 2002; Volume 356, pp. 385–393. [[CrossRef](#)]
17. Moghadam, M.M.; Rafiei, B.; Richoz, S.; Woods, A.D.; Krystyn, L. Anachronistic facies and carbon isotopes during the end-Permian biocrisis: Evidence from the mid-Tethys (Kisejin, Iran). *Palaeogeogra. Palaeoclimatol. Palaeoecol.* **2019**, *516*, 364–383. [[CrossRef](#)]
18. Chen, L.; Li, Y.; Cheng, Z. An overview of research and forecasting on rainfall associated with landfalling tropical cyclones. *Adv. Atmos. Sci.* **2010**, *27*, 967–976. [[CrossRef](#)]
19. Sun, Y.D.; Wignall, P.B.; Joachimski, M.M.; Bond, D.P.G.; Grasby, S.E.; Sun, S.; Yan, C.B.; Wang, L.N.; Chen, Y.L.; Lai, X.L. High amplitude redox changes in the late Early Triassic of South China and the Smithian-Spathian extinction. *Palaeogeogra. Palaeoclimatol. Palaeoecol.* **2015**, *427*, 62–78. [[CrossRef](#)]
20. Galfetti, T.; Bucher, H.; Martini, R.; Hochuli, P.A.; Weissert, H.; Crasquin-Soleau, S.; Guodun, K. Evolution of Early Triassic outer platform paleoenvironments in the Nanpanjiang Basin (South China) and their significance for the biotic recovery. *Sediment. Geol.* **2008**, *204*, 36–60. [[CrossRef](#)]
21. Zhang, T.S.; Chen, X.H.; Liu, Z.C. Seismites and Their Geological Significance in Early Triassic of Southeast Sichuan Basin. *Acta Sedimentol. Sin.* **2012**, *30*, 477–485. (In Chinese with English abstract)
22. Jamil, M.; Siddiqui, N.A.; Umar, M.; Ahmen, N.; Abdrahman, A.H.; Zaidi, F.K. Aseismic and seismic impact on development of soft-sediment deformation structures in deep-marine sand-shaly Crocker fan in Sabah, NW Borneo. *J. King Saud Univ. Sci.* **2021**, *33*, 101522. [[CrossRef](#)]
23. Jamil, M.; Siddiqui, N.A.; Ahmen, N.; Usman, M.; Umar, M.; Rahim, H.; Imran, Q.S. Facies analysis and sedimentary architecture of hybrid event beds in submarine lobes: Insights from the Crocker Fan, NW Borneo, Malaysia. *J. Mar. Sci. Eng.* **2021**, *9*, 1133. [[CrossRef](#)]
24. Zhao, Y.S.; Wang, D.Y.; Hu, Z.S. Sedimentology and Environment of Carbonate Gravity Flows on the Western Margin of Lower Triassic Sichuan Basin. *Acta Sedimentol. Sin.* **1994**, *12*, 1–8. (In Chinese with English abstract)
25. Jamil, M.; Siddiqui, N.A.; Usman, M.; Wahid, A.; Umar, M.; Ahmed, N.; Haq, I.U.; El-Ghali, M.A.K.; Imran, Q.S.; Rahman, A.H.A.; et al. Facies analysis and distribution of Late Palaeogene deep-water massive sandstones in submarine-fan lobes, NW Borneo. *Geol. J.* **2022**, *57*, 4489–4807. [[CrossRef](#)]

26. Lehrmann, D.J.; Wan, Y.; Wei, J.Y.; Yu, Y.Y.; Xiao, J.F. Lower Triassic peritidal cyclic limestone: an example of anachronistic carbonate facies from the Great Bank of Guizhou, Nanpanjiang Basin, Guizhou province, South China. *Palaeogeogr. Palaeoclimatol. Palaeoecol.* **2001**, *173*, 103–123. [[CrossRef](#)]
27. Shi, Z.Q.; Yi, H.S.; Zeng, D.Y.; Zhang, H. The lowest member of lower triassic feixianguan formation in upper yangtze region: Sedimentary records from sluggish water to turbulent ocean after the mass extinction. *Geo. Rev.* **2010**, *56*, 769–779. (In Chinese with English abstract)
28. Enos, P.; Jiayong, W.; Yangji, Y. Facies distribution and retreat of Middle Triassic Platform margin, Guizhou province, South China. *Sedimentology* **1997**, *44*, 563–584. [[CrossRef](#)]
29. Sun, S.; Li, J.; Chen, H.; Peng, H.; Hsu, K.J.; Shelton, J.W. Mesozoic and Cenozoic sedimentary history of South China. *AAPG Bull.* **1989**, *10*, 1247–1269.
30. Wang, Y.G.; Wen, Y.C.; Hong, H.T.; Xiao, M.L.; Fan, Y.; Wen, L.; Kong, L.X.; Wu, C.H. Carbonate slope facies sedimentary characteristics of the Late Permian to Early Triassic in northern Sichuan Basin. *J. Palaeogeogr.* **2009**, *11*, 143–156. (In Chinese with English abstract)
31. Huang, B.C.; Yan, Y.G.; Piper, J.D.A.; Zhang, D.H.; Yi, Z.Y.; You, S.; Zhou, T.H. Paleomagnetic constraints on the paleogeography of the East Asian blocks during late Paleozoic and early Mesozoic times. *Earth Sci. Rev.* **2018**, *186*, 8–36. [[CrossRef](#)]
32. Wignall, P.B.; Hallam, A.; Lai, X.L.; Yang, F.Q. Palaeoenvironmental changes across the Permian/Triassic boundary at Shangsi (Sichuan basin). *Histori. Biol.* **1995**, *10*, 175–189. [[CrossRef](#)]
33. Yuan, D.X.; Shen, S.Z.; Henderson, C.M.; Chen, J.; Zhang, H.; Zheng, Q.F.; Wu, H. Integrative timescale for the Lopingian (Late Permian): A review and update from Shangsi, South China. *Earth Sci. Rev.* **2019**, *188*, 190–209. [[CrossRef](#)]
34. He, B.; Zhong, Y.T.; Xu, Y.G.; Li, X.H. Triggers of Permo-Triassic boundary mass extinction in South China: The Siberian Traps or Paleo-Tethys ignimbrite flare-up? *Lithos* **2014**, *204*, 258–267. [[CrossRef](#)]
35. Kaihou, K.; Saito, R.; Ito, K.; Miyaji, T.; Biswas, R.; Tian, L.; Sano, H.; Shi, Z.Q.; Takahashi, S.; Tong, J.N.; et al. Effects of soil erosion and anoxic-euxinic ocean in the Permian-Triassic marine crisis. *Heliyon* **2016**, *2*, 00137. [[CrossRef](#)] [[PubMed](#)]
36. Galfetti, T.; Bucher, H.; Ovtcharova, M.; Schaltegger, U.; Brayard, A.; Brühwiler, T.; Goudemand, N.; Weissert, H.; Hochuli, P.A.; Cordey, F.; et al. Timing of the Early Triassic carbon cycle perturbations inferred from new U-Pb ages and ammonoid biochronozones. *Earth Planet. Sci. Lett.* **2007**, *258*, 593–604. [[CrossRef](#)]
37. Shen, S.Z.; Crowley, J.L.; Wang, Y.; Bowring, S.A.; Erwin, D.H.; Sadler, P.M.; Cao, C.Q.; Rothman, D.H.; Henderson, C.M.; Ramezani, J.; et al. Calibrating the end-Permian mass extinction. *Science* **2011**, *334*, 1367–1372. [[CrossRef](#)]
38. Zheng, B.S.; Mou, C.L.; Wang, X.P.; Chen, H.D.; Xiao, Z.H. Paleoclimate and paleoceanographic evolution during the Permian-Triassic transition (western Hubei area, South China) and their geological implications. *Palaeogeogr. Palaeoclimatol. Palaeoecol.* **2021**, *564*, 110166. [[CrossRef](#)]
39. Jiang, H.S.; Lai, X.L.; Yan, C.B.; Aldridge, R.J.; Wignall, P.B.; Sun, Y.D. Revised conodont zonation and conodont evolution across the Permian-Triassic boundary at the Shangsi section, Guangyuan, Sichuan, South China. *Glob. Planet. Chang.* **2011**, *77*, 103–115. [[CrossRef](#)]
40. Chen, Z.Q.; Yang, H.; Luo, M.; Benton, M.; Kaiho, K.; Zhao, L.S.; Huang, Y.G.; Zhang, K.X.; Fang, Y.H.; Jiang, H.S.; et al. Complete biotic and sedimentary records of the Permian-Triassic transition from Meishan section, South China: Ecologically assessing mass extinction and its aftermath. *Earth Sci. Rev.* **2015**, *149*, 67–107. [[CrossRef](#)]
41. Qiao, Z.F.; Janson, X.; Shen, A.J.; Zheng, J.F.; Zeng, H.L.; Wang, X.F. Lithofacies, architecture, and reservoir heterogeneity of tidal-dominated platform marginal oolitic shoal: An analogue of oolitic reservoirs of Lower Triassic Feixianguan Formation, Sichuan Basin, SW China. *Mar. Pet. Geol.* **2016**, *76*, 290–309. [[CrossRef](#)]
42. Qiao, Z.F.; Li, G.R.; Long, S.X.; Jiang, Z.Z.; Hu, W.Y.; Li, W.M. Characteristics and evolution model of sequence stratigraphy of Feixianguan Formation in the northeast of Sichuan Basin. *Acta Sedimentol. Sin.* **2010**, *28*, 462–470. (In Chinese with English abstract)
43. Li, F.; Gong, Q.L.; Burne, R.V.; Tang, H.; Su, C.P.; Zeng, K.; Zhang, Y.F.; Tan, X.C. Ooid factories operating under hothouse conditions in the earliest Triassic of South China. *Glob. Planet. Chang.* **2019**, *172*, 336–354. [[CrossRef](#)]
44. Rong, H.; Jiao, Y.; Wu, L.; Gu, Y.; Zhang, L. Relationship between heterogeneity and seismic velocities of the Yudongzi Triassic oolitic reservoirs in the Erlangmiao area, northwest Sichuan Basin, China. *J. Pet. Sci. Eng.* **2012**, *100*, 81–98. [[CrossRef](#)]
45. Tang, H.; Kershaw, S.; Liu, H.; Tan, X.C.; Li, F.; Hu, G.; Huang, C.; Wang, L.C.; Lian, C.B.; Li, L.; et al. Permian-Triassic boundary microbialites (PTBMs) in southwest China: Implications for paleoenvironment reconstruction. *Facies* **2016**, *63*, 2. [[CrossRef](#)]
46. Scotese, C.R.; Schettino, A. Late Permian–early Jurassic paleogeography of Western Tethys and the world. In *Permo-Triassic Salt Provinces of Europe, North Africa, and the Central Atlantic: Tectonics and Hydrocarbon Potential*; Soto, J.E., Linch, J.F., Tari, G., Eds.; Elsevier: Amsterdam, The Netherlands, 2017; Chapter 3; pp. 57–95.
47. Zhao, G.C.; Zhang, G.W.; Wang, Y.J.; Huang, B.C.; Dong, Y.P.; Li, S.Z.; Yu, S. Geological reconstructions of the East Asian blocks: From the breakup of Rodinia to the assembly of Pangea. *Earth Sci. Rev.* **2018**, *186*, 262–286. [[CrossRef](#)]
48. Dickson, J.A.D. A modified staining technique for carbonates in thin section. *Nature* **1965**, *205*, 587. [[CrossRef](#)]
49. Flügel, E. *Microfacies of Carbonate Rocks*; Springer: Berlin/Heidelberg, Germany; New York, NY, USA, 2004; pp. 680–716.
50. Dunham, R.J. Classification of carbonate rocks according to depositional texture. *Am. Assoc. Pet. Geol. Bull.* **1962**, *1*, 108–121.
51. Munnecke, A.; Wright, V.A.; Nohl, T. The origins and transformation of carbonate mud during early marine burial diagenesis and the fate of aragonite: A stratigraphic sedimentological perspective. *Earth Sci. Rev.* **2023**, *239*, 104366. [[CrossRef](#)]

52. Böhm, F.; Westphal, H.; Bornholdt, S. Required but disguised: Environmental signals in limestone-marl alternations. *Palaeogeogra. Palaeoclimatol. Palaeoecol.* **2003**, *189*, 161–178. [[CrossRef](#)]
53. Qiao, D.; Zhang, B.; Yin, H.; Duan, X.; Shi, Z.Q. Features and origin for calcirudites in the First Member of Feixianguan Formation in Guangyuan Area, Northwestern Sichuan Province. *Sediment. Geol. Tethys Geol.* **2022**. (In Chinese with English abstract) [[CrossRef](#)]
54. Sepkoski, J.J.; Bambach, R.K.; Droser, M.L. Secular changes in Phanerozoic event bedding and the biological overprint. In *Cycles and Events in Stratigraphy*; Einsele, G., Ricken, W., Seilacher, A., Eds.; Springer: Berlin, Germany, 1991; pp. 298–312.
55. Deev, E.V.; Zolnikov, I.D.; Gus' kov, S.A. Seismites in Quaternary sediments of southeastern Altai. *Russ. Geol. Geophys.* **2009**, *50*, 546–561. [[CrossRef](#)]
56. Kullberg, J.C.; Olo'riz, F.; Marques, B.; Caetano, P.S.; Rocha, R.B. Flat-pebble conglomerates: A local marker for Early Jurassic seismicity related to syn-rift tectonics in the Sesimbra area (Lusitanian Basin, Portugal). *Sediment. Geol.* **2001**, *139*, 49–70. [[CrossRef](#)]
57. Pratt, B.R.; Rule, R.G. A Mesoproterozoic carbonate platform (lower Belt Supergroup of western North America): Sediments, facies, tides, tsunamis and earthquakes in a tectonically active intracratonic basin. *Earth Sci. Rev.* **2021**, *217*, 103626. [[CrossRef](#)]
58. Morton, R.A.; Gelfenbaum, G.; Jaffe, B.E. Physical criteria for distinguishing sandy tsunami and storm deposits using modern examples. *Sediment. Geol.* **2007**, *200*, 184–207. [[CrossRef](#)]
59. Jaffe, B.; Gelfenbaum, G.; Rubin, D.; Peters, R.; Anima, R.; Swensson, M.; Olcese, D.; Bernales, L.; Gomez, J.; Riega, P. Tsunami deposits: Identification and interpretation of tsunami deposits from the June 23, 2001 Perú tsunami. In Proceedings of the International Conference on Coastal Sediments, Tampa, FL, USA, 18 May 2003.
60. Einsele, G.; Chough, S.K.; Shiki, T. Depositional events and their records—an introduction. *Sediment. Geol.* **1996**, *104*, 1–9. [[CrossRef](#)]
61. Shiki, T.; Yamazaki, T. The term “tsunamiite”. In *Tsunamiites*; Elsevier: Amsterdam, The Netherlands, 2008; pp. 5–8.
62. Costa, P.J.; Andrade, C. Tsunami deposits: Present knowledge and future challenges. *Sedimentology* **2020**, *67*, 1189–1206. [[CrossRef](#)]
63. Renne, P.R.; Zhang, Z.C.; Richards, M.A. Synchrony and causal relation between Permian-Triassic boundary crises and Siberian flood volcanism. *Science* **1995**, *269*, 1413–1416. [[CrossRef](#)] [[PubMed](#)]
64. Bowring, S.A.; Erwin, D.H.; Jin, Y.G. U/Pb zircon geochronology and tempo of the end-Permian mass extinction. *Science* **1998**, *280*, 1039–1045. [[CrossRef](#)]
65. Korte, C.; Pande, P.; Kalia, P.; Kozur, H.W.; Joachimski, M.M.; Oberhänsli, H. Massive volcanism at the Permian-Triassic boundary and its impact on the isotopic composition of the ocean and atmosphere. *J. Asian Earth Sci.* **2010**, *37*, 293–311. [[CrossRef](#)]
66. Duan, X. Geological Events during the Latest Permian to Earliest Triassic in the Upper Yangtze Region: Sedimentary Responses to the Disturbed Paleooceans. Ph.D. Thesis, Chengdu University of Technology, Chengdu, China, 2019.
67. Zhou, Y.Q.; Chai, Z.F.; Ma, J.G.; Kong, P.; Fu, G.M. Preliminary study on iron pellets in P/T boundary clay at Shangsi, Guangyuan, Sichuan. *Chin. Sci. Bull.* **1988**, *33*, 397–398. (In Chinese with English abstract)
68. Miono, S.; Chengzhi, Z.; Nakayama, Y. Study of microspherules in the Permian-Triassic bedded chert of the Sasayama section, southwest Japan by PIXE analysis. *Nucl. Instrum. Methods Phys. Res. Sect. B Beam Interact. Mater. At.* **1996**, *109*, 612–616. [[CrossRef](#)]
69. Lana, C.; Marangoni, Y. The Araguinha impact: A south American permo-triassic catastrophic event. *Geol. Today* **2009**, *25*, 21–28. [[CrossRef](#)]
70. Becker, L.; Poreda, R.J.; Hunt, A.G.; Bunch, T.E.; Rampino, M. Impact event at the Permian-Triassic boundary: Evidence from extraterrestrial noble gases in fullerenes. *Science* **2001**, *291*, 1530–1533. [[CrossRef](#)]
71. Becker, L.; Poreda, R.J.; Basu, A.R.; Pope, K.O.; Harrison, T.M.; Nicholson, C.; Iasky, R. Bedout: A possible end-Permian impact crater offshore of northwestern Australia. *Science* **2004**, *304*, 1469–1476. [[CrossRef](#)]
72. Basu, A.R.; Petaev, M.I.; Poreda, R.J.; Jacobsen, S.B.; Becker, L. Chondritic meteorite fragments associated with the Permian-Triassic boundary in Antarctica. *Science* **2003**, *302*, 1388–1392. [[CrossRef](#)]
73. Koeberl, C.; Farley, K.A.; Peucker-Ehrenbrink, B.; Sephton, M.A. Geochemistry of the end-Permian extinction event in Austria and Italy: No evidence for an extraterrestrial component. *Geology* **2004**, *32*, 1053–1056. [[CrossRef](#)]
74. Woods, A.D. Paleoceanographic and paleoclimatic context of Early Triassic time. *C. R. Palevol.* **2005**, *4*, 463–472. [[CrossRef](#)]
75. Preto, N.; Kustatscher, E.; Wignall, P.B. Triassic climates—state of the art and perspectives. *Palaeogeogra. Palaeoclimatol. Palaeoecol.* **2010**, *290*, 1–10. [[CrossRef](#)]
76. Ito, M.; Ishigaki, A.; Nishikawa, T.; Saito, T. Temporal variation in the wavelength of hummocky cross-stratification: Implications for storm intensity through Mesozoic and Cenozoic. *Geology* **2001**, *29*, 87–89. [[CrossRef](#)]
77. Guardado-France, R.; Johnson, M.E.; Ledesma-Vázquez, J.; Miguel, A.; Rio, S.R.; Herrera-Gutiérrez, A.R. Multiphase Storm Deposits Eroded from Andesite Sea Cliffs on Isla San Luis Gonzaga (Northern Gulf of California, Mexico). *J. Mar. Sci. Eng.* **2020**, *8*, 525. [[CrossRef](#)]
78. Chen, J.T.; Han, Z.Z.; Zhang, X.L.; Fan, A.P.; Yang, R.C. Early diagenetic deformation structures of the Furongian ribbon rocks in Shandong Province of China—A new perspective of the genesis of limestone conglomerates. *Sci. China Earth Sci.* **2010**, *53*, 241–252. [[CrossRef](#)]
79. Kidder, D.L.; Worsley, T.R. Causes and consequences of extreme Permo-Triassic warming to globally equable climate and relation to the Permo-Triassic extinction and recovery. *Palaeogeogra. Palaeoclimatol. Palaeoecol.* **2004**, *203*, 207–237. [[CrossRef](#)]
80. Bottjer, D.J. Life in the early triassic ocean. *Science* **2012**, *338*, 336–337. [[CrossRef](#)] [[PubMed](#)]

81. Wei, H.Y.; Shen, J.; Schoepfer, S.D.; Krystyn, L.; Richoz, S.; Algeo, T.J. Environmental controls on marine ecosystem recovery following mass extinctions, with an example from the Early Triassic. *Earth Sci. Rev.* **2015**, *149*, 108–135. [[CrossRef](#)]
82. Parrish, J.T. Climate of the supercontinent Pangea. *J. Geol.* **1993**, *101*, 215–233. [[CrossRef](#)]
83. Jelby, M.E.; Grundvag, S.A.; Hamsen, W.H.; Olaussen, S.; Stemmerik, L. Tempestite facies variability and storm-depositional processes across a wide ramp: Towards a polygenetic model for hummocky cross-stratification. *Sedimentology* **2020**, *67*, 742–781. [[CrossRef](#)]
84. Myrow, P.M.; Tice, L.; Archuleta, B.; Clark, B.; John, F.; Taylors, R.L. Flat-pebble conglomerate: Its multiple origins and relationship to metre-scale depositional cycles. *Sedimentology* **2004**, *51*, 973–996. [[CrossRef](#)]
85. Okubo, J.; Warren, L.V.; Luvizotto, G.L.; Varejão, F.G.; Quaglio, F.; Uhlein, G.J.; Assine, M.L. Evidences of seismic events during the sedimentation of Sete Lagoas Formation (Bambuí Group-Ediacaran, Brazil). *J. South. Am. Earth Sci.* **2020**, *98*, 102461. [[CrossRef](#)]
86. Kwon, Y.K.; Chough, S.K.; Choi, D.K.; Lee, D.J. Origin of limestone conglomerates in the Choson Supergroup (Cambro-Ordovician), mid-east Korea. *Sediment. Geol.* **2002**, *146*, 265–283. [[CrossRef](#)]
87. Chough, S.K.; Kwon, Y.K.; Choi, D.K.; Lee, D.J. Autoconglomeration of limestone. *Geosci. J.* **2001**, *5*, 159–164. [[CrossRef](#)]
88. Kershaw, S.; Crasquin, S.; Collin, P.Y.; Li, Y.; Feng, Q.; Forel, M.B. Microbialites as disaster forms in anachronistic facies following the end-Permian mass extinction: A discussion. *Aust. J. Earth Sci.* **2009**, *56*, 809–813. [[CrossRef](#)]
89. Iozaki, Y. Permo-Triassic boundary superanoxia and stratified superocean: Records from the lost deep sea. *Science* **1997**, *276*, 235–238. [[CrossRef](#)]
90. Tavakoli, V.; Bonab, H.R. Uranium depletion across Permian-Triassic Boundary in Persian Gulf and its implications for paleo-oceanic conditions. *Palaeogeogra. Palaeoclimatol. Palaeoecol.* **2012**, *350*, 101–113. [[CrossRef](#)]
91. Koeshidayatullah, A.; Khalid, R.A.; Li, X.W.; Lehrmann, D.J.; Trower, E.J.; Morsilli, M.; Mukerji, T.; Payne, J.L. Quantitative evaluation of the roles of ocean chemistry and climate on ooid size across the Phanerozoic: Global versus local controls. *Sedimentology* **2022**, *69*, 2486–2506. [[CrossRef](#)]
92. Cox, R.; Boyle, L.; Cytrynbaum, J. Imbricated Coastal Boulder Deposits are Formed by storm waves, and can preserve a Longterm storminess Record. *Nature* **2019**, *9*, 10784.
93. Jiang, L.; Worden, R.H.; Cai, C.F.; Shen, A.J.; He, X.Y.; Pan, L.Y. Contrasting diagenetic evolution patterns of platform margin limestones and dolostones in the Lower Triassic Feixianguan Formation, Sichuan Basin, China. *Mar. Petro. Geol.* **2018**, *92*, 332–351. [[CrossRef](#)]
94. Reijmer, J.J.G.; Mulder, T. Carbonate slopes and gravity deposits. *Sediment. Geol.* **2015**, *317*, 1–8. [[CrossRef](#)]
95. Tian, J.; Wu, S.G.; Fuliang, L.; Wang, D.W.; Wang, B.; Zhang, X.Y.; Ma, B.J. Middle Miocene mound-shaped sediment packages on the slope of the Xisha carbonate platforms, South China Sea: Combined result of gravity flow and bottom current. *Deep Sea Res. Part II Top. Stud. Ocean.* **2015**, *122*, 172–184. [[CrossRef](#)]

**Disclaimer/Publisher’s Note:** The statements, opinions and data contained in all publications are solely those of the individual author(s) and contributor(s) and not of MDPI and/or the editor(s). MDPI and/or the editor(s) disclaim responsibility for any injury to people or property resulting from any ideas, methods, instructions or products referred to in the content.